

University of Dayton

eCommons

---

Electro-Optics and Photonics Faculty  
Publications

Department of Electro-Optics and Photonics

---

12-1-2020

## Polarization-selective modulation of supercavity resonances originating from bound states in the continuum

Chan Kyaw  
*Howard University*

Riad Yahiaoui  
*Howard University*

Joshua A. Burrow  
*University of Dayton*

Viet Tran  
*Howard University*

Kyron Keelen  
*Morehouse College*

Below this page for additional works that [https://ecommons.udayton.edu/eop\\_fac\\_pub](https://ecommons.udayton.edu/eop_fac_pub)



Part of the [Electromagnetics and Photonics Commons](#), [Optics Commons](#), and the [Other Physics Commons](#)

---

### eCommons Citation

Kyaw, Chan; Yahiaoui, Riad; Burrow, Joshua A.; Tran, Viet; Keelen, Kyron; Sims, Wesley; Red, Eddie C.; Rockward, Willie S.; Thomas, Mikkel A.; Sarangan, Andrew M.; Agha, Imad; and Searles, Thomas A., "Polarization-selective modulation of supercavity resonances originating from bound states in the continuum" (2020). *Electro-Optics and Photonics Faculty Publications*. 127.  
[https://ecommons.udayton.edu/eop\\_fac\\_pub/127](https://ecommons.udayton.edu/eop_fac_pub/127)

This Article is brought to you for free and open access by the Department of Electro-Optics and Photonics at eCommons. It has been accepted for inclusion in Electro-Optics and Photonics Faculty Publications by an authorized administrator of eCommons. For more information, please contact [mschlengen1@udayton.edu](mailto:mschlengen1@udayton.edu), [ecommons@udayton.edu](mailto:ecommons@udayton.edu).

---

**Author(s)**

Chan Kyaw, Riad Yahiaoui, Joshua A. Burrow (0000-0002-1237-4662), Viet Tran, Kyron Keelen, Wesley Sims, Eddie C. Red, Willie S. Rockward, Mikkel A. Thomas, Andrew M. Sarangan, Imad Agha, and Thomas A. Searles

## Polarization-selective modulation of supercavity resonances originating from bound states in the continuum

Chan Kyaw<sup>1</sup>, Riad Yahiaoui<sup>1</sup>, Joshua A. Burrow<sup>2</sup>, Viet Tran<sup>1</sup>, Kyron Keelen<sup>3</sup>, Wesley Sims<sup>3</sup>, Eddie C. Red<sup>3</sup>, Willie S. Rockward<sup>4</sup>, Mikkel A. Thomas<sup>5</sup>, Andrew Sarangan<sup>2</sup>, Imad Agha<sup>2</sup> & Thomas A. Searles<sup>1</sup>✉

Bound states in the continuum (BICs) are widely studied for their ability to confine light, produce sharp resonances for sensing applications and serve as avenues for lasing action with topological characteristics. Primarily, the formation of BICs in periodic photonic band gap structures are driven by symmetry incompatibility; structural manipulation or variation of incidence angle from incoming light. In this work, we report two modalities for driving the formation of BICs in terahertz metasurfaces. At normal incidence, we experimentally confirm polarization driven symmetry-protected BICs by the variation of the linear polarization state of light. In addition, we demonstrate through strong coupling of two radiative modes the formation of capacitively-driven Freidrich-Wintgen BICs, exotic modes which occur in off- $\Gamma$  points not accessible by symmetry-protected BICs. The capacitance-mediated strong coupling at  $0^\circ$  polarization is verified to have a normalized coupling strength ratio of 4.17% obtained by the Jaynes-Cummings model. Furthermore, when the polarization angle is varied from  $0^\circ$  to  $90^\circ$  ( $0^\circ \leq \phi < 90^\circ$ ), the Freidrich-Wintgen BIC is modulated until it is completely switched off at  $90^\circ$ .

<sup>1</sup>Department of Physics and Astronomy, Howard University, Washington, DC 20059, USA. <sup>2</sup>Electro-Optics Department, University of Dayton, Dayton, OH 45469, USA. <sup>3</sup>Department of Physics & Dual-Degree Engineering, Morehouse College, Atlanta, GA 30314, Georgia. <sup>4</sup>Department of Physics, Morgan State University, Baltimore, MD, USA. <sup>5</sup>Institute for Electronics and Nanotechnology, Georgia Institute of Technology, Atlanta, GA 30332, USA.  
✉email: [thomas.searles@howard.edu](mailto:thomas.searles@howard.edu)

The concept of bound states in the continuum, or BIC, was first proposed by von Neumann and Wigner for an electron in an artificial complex potential<sup>1</sup>. Thereafter, different types of BICs have been reported in quantum systems<sup>2,3</sup>, acoustic and water waves<sup>4,5</sup> and photonic systems<sup>6–12</sup>, where modes inside the radiation continuum above the light line are perfectly confined instead of radiating away. Due to the infinite quality (Q-) factor and zero linewidth of the BIC modes, only quasi-BICs with partial confinement and finite linewidth are observed experimentally. The partial confinement of waves has applications in lasing<sup>13–16</sup>, nonlinear phenomena<sup>17–20</sup> and high-performance sensing devices<sup>21–23</sup>.

In general, bound states in the continuum originate from two physical mechanisms. The more common type, symmetry-protected (SP-) BIC results from a symmetry mismatch between radiative modes and the mode profiles inside the Brillouin zone near the  $\Gamma$  point. The second classification, Friedrich–Wintgen (FW-) BICs (or accidental BICs), originates from destructive interference between two radiation modes modulated by a specific parameter<sup>24</sup>. Unlike SP-BICs, FW-BICs are observed at off- $\Gamma$  points in regions with an accidental symmetry. These regions of the band dispersion result in extremely high Q factors around the FW-BIC, called near-BIC<sup>25</sup> or supercavity resonances<sup>13,26</sup>, and are attributed to the coupling strength of the two radiative modes that interfere destructively. The position and Q factor of the supercavity resonances can be extremely sensitive to structural parameters of the device<sup>27</sup>. Furthermore, in accordance with FW-BIC theory, changes in the coupling strength of the resonances result in a shift of the FW-BIC positions in the band dispersion<sup>24,28</sup>. Efficient control of the position and Q factor of the supercavity resonance is desirable for practical design of high Q-factor devices.

Limited experimental demonstrations of FW-BICs have been shown to be dependent on angles of incident radiation in the infrared regime<sup>10,25,29</sup>. At terahertz (THz) frequencies, SP-BICs<sup>30–32</sup> with few realizations of FW-BICs<sup>26,33</sup> have been reported. Recent investigations by Han et al.<sup>26</sup> reported resonance-trapped BICs with similar mechanism as FW-BICs for THz metasurfaces by tailoring the geometric lengths of the silicon resonators. They also reported frequency and Q-factor modulation of the supercavity resonance through optical pumping of the silicon resonators. Furthermore, Pankin et al.<sup>34</sup> reported FW-BICs at particular linear polarization angles in one-dimensional PhC structure with anisotropic defect layer (ADL). The FW-BIC in the structure is formed by complete destructive interference of the extraordinary and ordinary waves at the output from the ADL.

In this Article, we report the modulation of both types of BIC driven by two unique modalities: linear polarization state of light for SP-BIC and through capacitance-mediated strong coupling for FW-BIC. We then investigate the influence of polarization state of the light on FW-BIC formation. The results of this work provide an active methodology to manipulate the extremely high Q-factor resonances of BICs via manipulation of the incoming radiation or capacitive gaps of split-ring resonator (SRR) structure which could be advantageous for photonic, lasing, and sensing applications. The paper is organized as follows. First, we confirm that a quasi-BIC is formed by breaking the symmetry of the SRR unit cell. Next, we investigate the influence of polarization on the transmission spectra of the terahertz metasurface at highest asymmetry, where a SP-BIC is formed at 30°. Then, we demonstrate through modulation of the capacitive gap, the phenomenon of FW-BIC in an asymmetric SRR from strong coupling between the radiative plasmonic dipole mode and higher order quadrupole mode. Finally, to investigate the polarization dependence of FW-BIC formation, we vary the polarization angle

of incident light from 0° to 90° (0° ≤  $\phi$  < 90°). Notably, the FW-BIC decreases gradually with increasing polarization angle until FW-BIC is completely switched off at 90°.

## Results

SP-BICs can be verified by breaking the structural symmetry of the device. Here, we experimentally show the quasi-BICs originating from the translation of the top gap of the unit cell, confirming the results of Cong and Singh<sup>30</sup>. In general, any small perturbation of the BIC including off-normal incidence (Supplementary Note 1) gives rise to quasi-BICs that can be experimentally verified such that SP bound states can radiate through coupling with the incoming radiation.

The unit cell geometry of an asymmetric SRR with four capacitive gaps at  $\delta = 72.5 \mu\text{m}$  is shown in Fig. 1a. The dimensions are length  $l$  of 250  $\mu\text{m}$ , bracket width  $w$  of 35  $\mu\text{m}$  and capacitive gap width  $c$  of 35  $\mu\text{m}$  arranged in an array with 300  $\mu\text{m}$  period. An asymmetry parameter,  $\alpha$  has been defined as 100% ×  $\delta_i/\delta_{\text{max}}$  where  $\delta_i$  is the distance between the gap center and the symmetry line and  $\delta_{\text{max}}$  is 72.5  $\mu\text{m}$ . Experimentally, the SRR arms consist of 100 nm thick silver layer deposited by radiofrequency sputtering on polyimide substrate of 50.8  $\mu\text{m}$  thickness using conventional lithography. An optical microscope image of the metasurface is also shown in Fig. 1b.

As shown in Fig. 1a, the top gap is translated laterally toward the right to break the  $C_4$  symmetry and produce quasi-BICs in the form of a Fano resonance lineshape<sup>35–41</sup>. The asymmetry parameter  $\alpha$ , defined previously, describes a general parameter common to all SP-BICs. The simulated and experimental transmission spectra are plotted when the incident radiation is horizontally polarized ( $x$ -pol) in Fig. 2a versus vertically polarized ( $y$ -pol) in Fig. 2b. The transition from a SP-BIC to a quasi-BIC, due to asymmetry, is observed for both experiment and simulation in  $x$ - and  $y$ -polarizations. The degree of asymmetry before quasi-BICs can be detected is larger for  $x$ -polarization where the transmission dip only becomes visible in simulations around 11% as compared to 3% asymmetry for  $y$ -polarization.

The extremely sharp quasi-BICs produced by very small perturbations are not resolved experimentally due to scattering losses from slight imperfections and defects in the sample. The quasi-BIC closest to SP-BIC modes are observed experimentally at  $\alpha = 40\%$  for  $x$ -polarization and at  $\alpha = 20\%$  for  $y$ -polarization. The inserts inside transmission graphs plotted in Fig. 2a, b show the quasi-BICs in more detail. The spectral feature of quasi-BIC also broadens with increasing asymmetry showing a strong dependence on asymmetric gap distance.

Further evidence of SP-BIC is represented by the disappearance of a resonance at the symmetry restoring region, where the linewidth becomes zero or quality factor tends to infinity<sup>10,42</sup>. The Q factors of the resonances are calculated as  $Q = \omega_0/2\gamma$  where  $\omega_0$  is center resonance frequency and  $\gamma$  is damping rate of the resonance extracted from the equation below<sup>12</sup>

$$T(w) = a_1 + ia_2 + \frac{b}{\omega - \omega_0 + i\gamma}, \quad (1)$$

where  $a_1$ ,  $a_2$ , and  $b$  are constant real numbers. The calculated Q factors are then fitted by a  $Q \propto \alpha^{-2}$  curve<sup>30</sup>. In Fig. 2c, d, the calculated Q factors of quasi-BICs show a clear diverging trend when the structure approaches symmetry. However, the Q-factor diverges closer to the symmetric region for  $y$ -polarization. This shows the incident field is more sensitive to the asymmetry in the structure when the electric field is orientated perpendicular to the translated gap. The experimentally measured Q-factor values are resolved for higher degree of asymmetry with 23.7 for  $x$ -polarization and 17.2 for  $y$ -polarization at  $\alpha = 40\%$ . The extracted

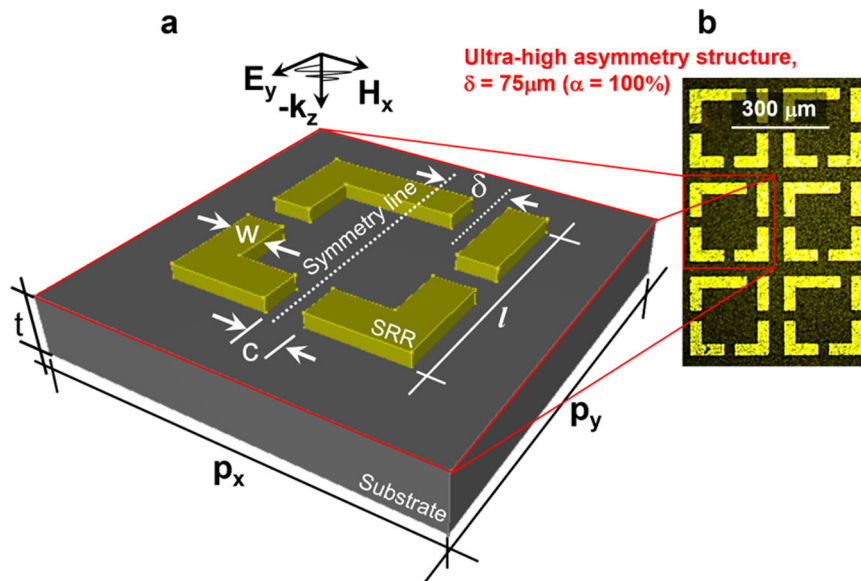


**Fig. 1 Schematic of unit cell geometry of the asymmetric THz metasurface array.** **a** Geometrical description of the asymmetric split-ring resonator (SRR) unit cell with length ( $l$ ) = 250  $\mu\text{m}$ , bracket width ( $w$ ) = 35  $\mu\text{m}$ , capacitive gap width ( $c$ ) = 35  $\mu\text{m}$ , thickness ( $t$ ) = 50.8  $\mu\text{m}$ , gap distance ( $\delta$ ) = 72.5  $\mu\text{m}$  or asymmetry parameter ( $\alpha$ ) = 100%, and its respective optical image (**b**). The arrows indicate the directions of the electric field ( $E_y$ ), magnetic field ( $H_x$ ), and propagation ( $k_z$ ).

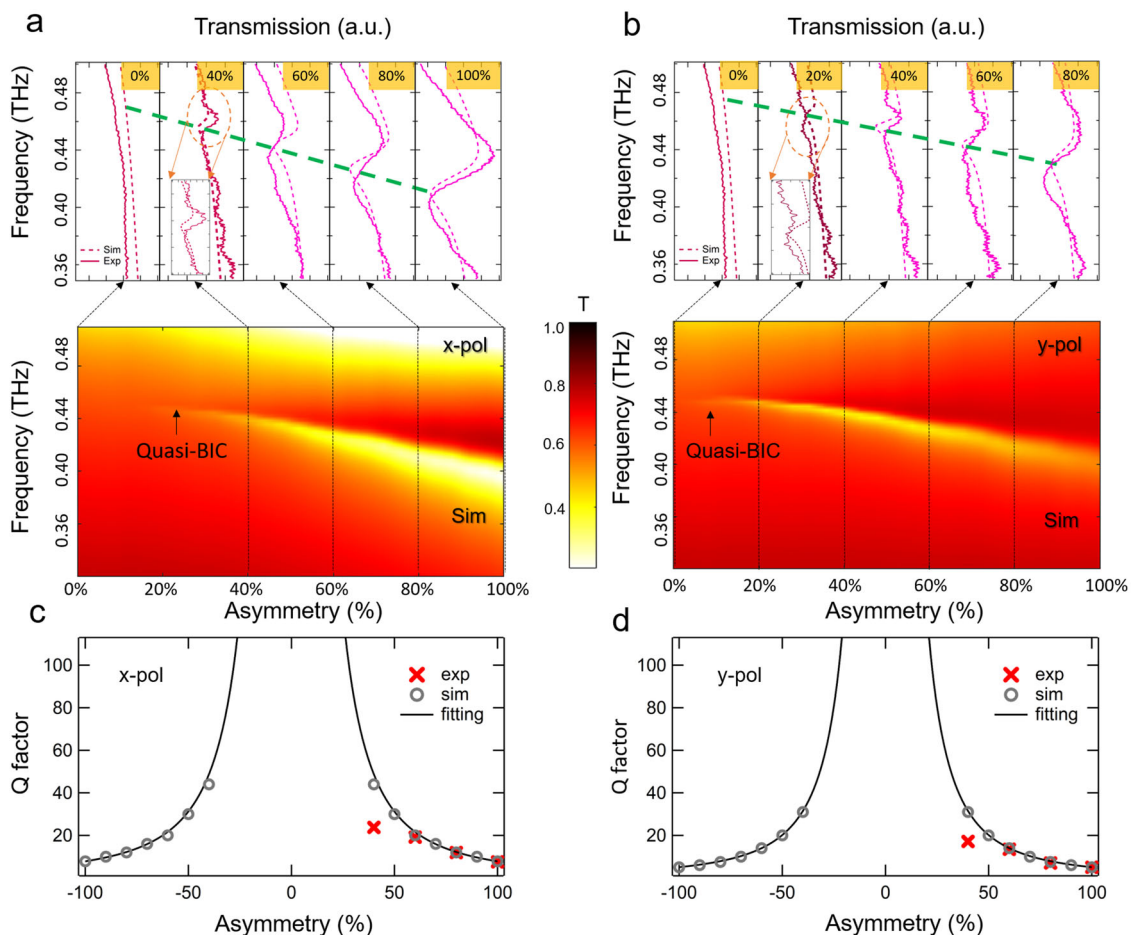


**Fig. 2 Experimental and numerical investigation of the symmetry-protected bound states in the continuum (BICs) from quasi-BICs induced by top gap translation.** Transmission ( $T$ ) spectra from experiment (exp) and simulation (sim) for **(a)** horizontal polarization (x-pol), **(b)** vertical polarization (y-pol) with respective pictorial illustrations with dependence on asymmetry parameter ( $\alpha$ ) to exhibit the BIC nature from disappearance of the Fano at symmetric region. The quality (Q-) factors for **(c)** x-pol and **(d)** y-pol BIC resonances as a function of  $\alpha$  are fitted with  $Q \propto \alpha^{-2}$ . Under similar conditions of measurement, error bars are smaller than data points and are imperceptible to be represented here.

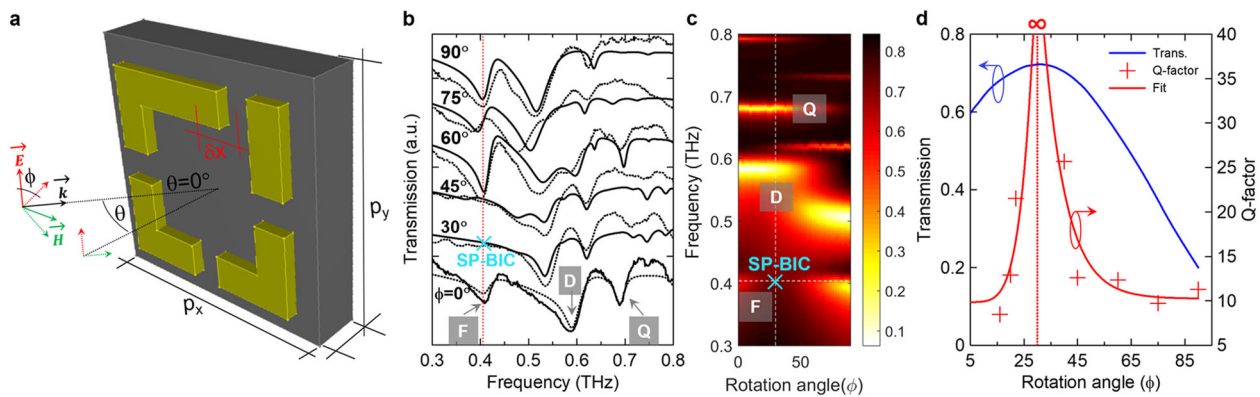


**Fig. 3 Investigation for the polarization-driven modulation of symmetry-protected bound states in the continuum.** **a** Unit cell of an array with periodicity ( $p_x$  or  $p_y$ ) for the ultrahigh asymmetry sample where the asymmetry parameter,  $\alpha = 100\%$ . The arrows indicate the directions of the electric field ( $E$ ), magnetic field ( $H$ ), and propagation ( $k$ ) vector incident on the sample surface at an angle  $\theta$ . **b** Experimental (dashed lines) and simulated (solid lines) transmission spectra for different rotational angles  $\phi$  corresponding to different linear polarization states confirm the complete disappearance of the Fano mode at  $\phi = 30^\circ$  due to SP-BIC. **c** Contour plot illustrating the transmission amplitude for different rotational angles between  $0^\circ$  and  $90^\circ$ , respectively, and within 0.3 and 0.8 THz with the cross symbol indicating the SP-BIC position with vanishing linewidth. **d** Transmission (Trans.) amplitude and quality (Q-) factor of the Fano resonance near 0.4 THz calculated from the simulated transmission spectra are plotted as a function of rotation angle  $\phi$ . The transmission peak indicates the SP-BIC point induced by rotation. Under similar conditions of simulation, error bars are smaller than data points and are imperceptible to be represented here.

experimental Q factors of the resonances show good agreement with the simulated curves. Furthermore, the Q-factor values presented here are comparable to the literature values for THz metasurfaces of asymmetric resonances reported from 20 to 79<sup>30,38,39,43–45</sup>.

To understand the dependence of incident polarization, the ultrahigh asymmetry sample ( $\alpha = 100\%$ ) was measured for angle  $\phi$  rotated counter-clockwise from  $0^\circ$  to  $90^\circ$  to mimic different linear polarization states; as illustrated in Fig. 3a. The resulting spectra for different rotation angles are plotted in Fig. 3b with the accompanying simulated spectra, where  $\phi$  in that case corresponds to the polarization angle of the incoming THz wave. The measured Fano resonance disappears when the sample is rotated to  $\phi = 30^\circ$  and reappears at  $\phi = 45^\circ$ . This behavior is attributed to the phenomenon of SP-BIC. In a symmetric unit cell, the  $x$  and  $y$  components of the electric field cancel out such that the overlap integral is zero with respect to any polarization state of the incident beam and thus forming SP-BIC. Meanwhile for our asymmetric sample, the sample rotation alters the mode profile such that the overlap integral is 0 for a polarization angle of  $30^\circ$  resulting in the disappearance of the Fano mode to form SP-BIC.

A colormap for simulated amplitude as a function of incident polarization angle is presented in Fig. 3c. The Fano, dipole, and quadrupole modes are denoted as F, D, and Q respectively in the figure. Furthermore, the simulated transmission amplitude and Q factor of the Fano dip are plotted as a function of rotation angle in Fig. 3d. The transition from Fano to SP-BIC and back to a Fano-type resonance can be observed in the transmission amplitude with a peak at  $\phi = 30^\circ$  in Fig. 3d. This angle represents the SP-BIC point with vanishing linewidth as described by a cross in pictorial illustration of Fig. 3c. The Q factor also becomes infinite as the rotational angles approach the SP-BIC point near  $\phi = 30^\circ$  as seen in Fig. 3d.

In previous studies, SP-BICs occurred at nonzero incidence angles<sup>30,32</sup> and through geometric manipulation<sup>30,31</sup>. The SP-BIC experimentally observed in our system is driven by tuning the linear polarization states of electromagnetic field at normal incidence on the sample. This allows for a polarization selective method to produce the SP-BIC in an asymmetric sample through polarization engineering. The advantage of EM waves is the scalability of optical responses to different frequency bands.

Therefore, we can take advantage of this result to induce the polarization selective SP-BICs in other deep subwavelength regions by tailoring the metasurface geometry.

## Discussion

A noteworthy feature in the transmission spectra of Fig. 3b is the splitting of the dipole resonance into two distinct resonance dips. This occurs for a polarization angle  $\theta$  between  $45^\circ$  and  $60^\circ$  approximately. Further numerical calculations and analysis have shown that this mode splitting is accompanied by a strong cross-polarized component  $t_{yx}$  (Supplementary Note 2).

At  $0^\circ$  incident polarization angle (Fig. 3b,  $\phi = 0^\circ$ ) one can observe three main dips in the transmission spectrum around 0.4, 0.58, and 0.69 THz, respectively with a good agreement between simulation and experiment. In order to get an insight into the nature of the resonances, we simulate the surface current distribution at the aforementioned resonances (Fig. 4a–c). When the symmetry of the structure is broken with the increase of the parameter  $\delta$ , the lengths of the right and left arms of the SRRs are no longer equal and the electric dipole moments of the coupled SRRs arms differ from each other. The coupling of these two different dipole modes leads to the emergence of two asymmetric Fano line shapes around 0.4 and 0.69 THz, respectively for the 100% of asymmetry case (i.e.,  $\alpha = 72.5 \mu\text{m}$ ). For the sharp asymmetric resonance at 0.4 THz, denoted as F in Fig. 3b, we observe anti parallel currents in the right and left arcs (Fig. 4a). This resonance mode is similar in nature to the inductive capacitive (LC) resonance in a single gap SRR as both resonances result in current configurations that give rise to a magnetic dipole moment perpendicular to the metamaterial plane of the array.

The distinct surface current distribution profiles of the remaining resonances that appear around 0.58 and 0.69 THz suggest the excitation of dipole and quadrupole modes, denoted as D and Q, respectively in Fig. 3b. The dipole resonance at  $\sim 0.58$  THz is attributed to the excitation of dipole-like plasmons in the vertical arms of the SRRs, where the currents are parallel to the polarization of the electric field. The current distribution as seen in Fig. 4b radiates strongly to the free space giving rise to a broader resonance in the transmission spectrum. The quadrupole resonance is observed at 0.69 THz. The four arrows show how the

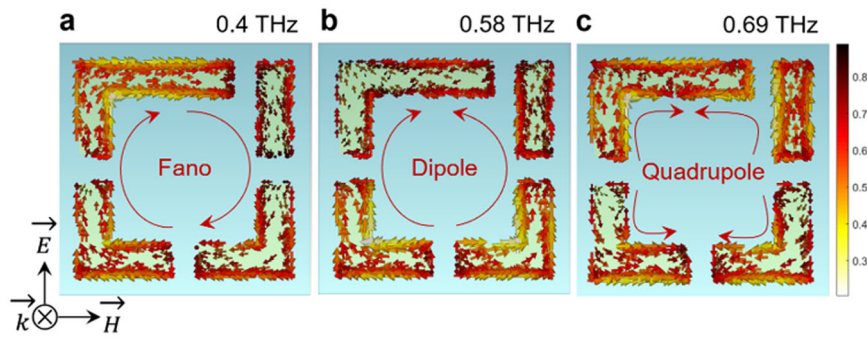


**Fig. 4 Surface current distribution at resonant frequencies.** **a** Fano mode resonance, **b** dipole resonance, and **c** quadrupole resonance at 0.4, 0.58, and 0.69 THz, respectively, for asymmetry parameter  $\alpha = 100\%$  where the colourscale represents normalized current intensity. The red arrows on the surface of each unit cell indicate instantaneous directions of the current flow at certain phase shifts. The black arrows in the bottom left represent the directions of the electric field ( $E$ ), magnetic field ( $H$ ), and propagation ( $k$ ) vectors.

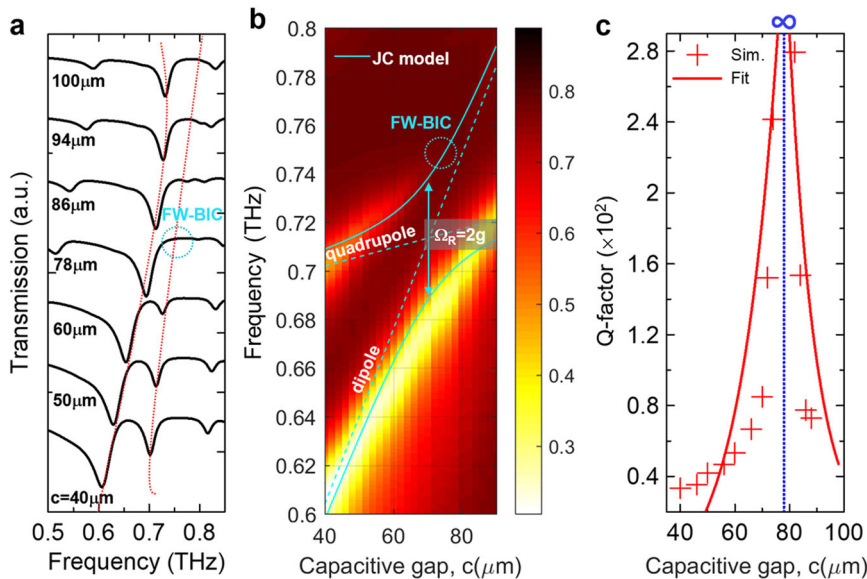


**Fig. 5 Investigation of the capacitively-driven Friedrich-Wintgen (FW-) bound states in the continuum (BICs).** **a** Simulated transmission spectra for different capacitive gap “ $c$ ”, showing an avoided crossing and linewidth vanishing due to the hybridization of dipole and quadrupole modes. The dotted circle indicates the FW-BIC position with vanishing linewidth. **b** Contour plot illustrating the transmission amplitude for different values of the capacitive gap between 40 and 100  $\mu\text{m}$  respectively. A fit was applied to the data with Jaynes-Cummings (JC) Hamiltonian to calculate Rabi splitting parameter,  $\Omega_R$ . **c** Quality (Q-) factor vs. capacitive gap calculated from simulation (Sim) data. The FW-BIC appears at  $c = 78 \mu\text{m}$  where  $Q$  approaches  $\infty$ . Under similar conditions of simulation, error bars are smaller than data points and are imperceptible to be represented here.

current distribution behaves in general. There are two sets of out of phase current distribution. Introducing the asymmetry leads to this kind of current distribution that scatters the electromagnetic field very weakly and dramatically reduces the coupling to the free space, thus causing a huge reduction in the radiation losses which eventually leads to very sharp resonance. The quadrupole resonance is inaccessible in the symmetrical structure<sup>40</sup>.

In contrast to SP-BIC, FW-BIC appears due to destructive interference of the resonances at the correct phase matching conditions<sup>24</sup>. This type of bound states is also sometimes referred to as “an accidental” BIC<sup>25,46</sup>. When two resonances approach each other as a function of a certain parameter, interferences cause an anticrossing of the two resonances in their frequency/energy positions and for a certain value of the parameter, the width of one of the resonances may vanish, thus leading to the generation of a BIC. In this context, by simultaneously altering the width of the capacitive gaps of the structure with 100% of asymmetry, it is possible to strongly couple the radiative

plasmonic dipole mode and the higher order quadrupole mode to form a BIC, as illustrated in Fig. 5.

The simulated transmission coefficients at different widths of the capacitive gaps are plotted in Fig. 5a illustrating an avoided crossing behavior. In the absence of strong coupling, the dispersion of the involved modes will merely cross each other at a specific width of the capacitive gaps, namely  $c = 78 \mu\text{m}$ . However, due to the strong coupling regime, an avoided resonances crossing is observed with a Rabi splitting  $\Omega_R$  and a normalized coupling strength ratio  $g = \Omega_R/2\omega_d$  of about 4.17% (Fig. 5b). This hybrid dispersion state is accompanied by a vanishing of the spectral quadrupole line at  $c = 78 \mu\text{m}$  which is a distinct feature of the FW-BIC.

The Q factor of the FW-BIC is plotted in Fig. 5c. At the FW-BIC point, the Q-factor diverges to infinity due to absence of losses<sup>25</sup>. This is characteristic of a FW-BIC arising from destructive interference between radiative modes modulated by a specific parameter. The resonances with high Q-factor

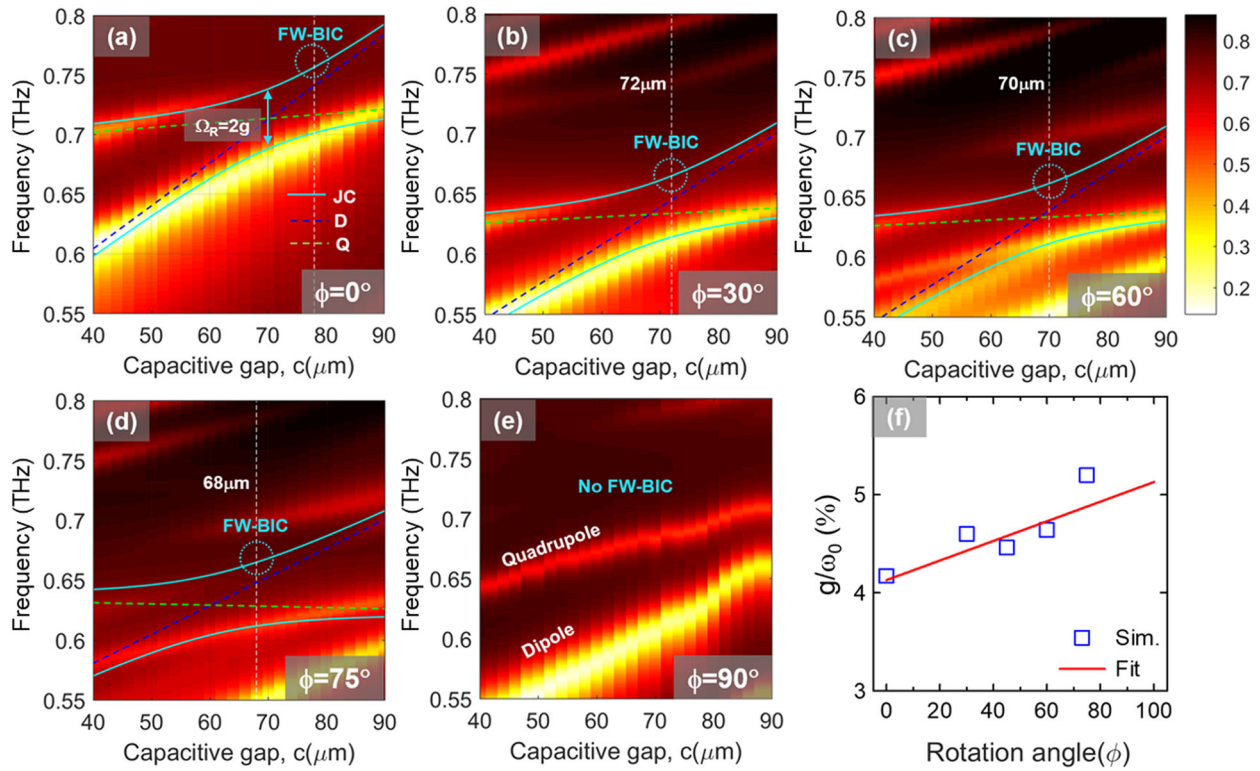


**Fig. 6 Polarization-dependence for capacitively-driven Friedrich-Wintgen (FW-) bound states in the continuum (BICs).** **a–e** Contour plot illustrating the transmission amplitude for different values of the rotation angle  $\phi$  between  $0^\circ$  and  $90^\circ$ , respectively. The white vertical dashed lines indicate the FW-BIC positions with vanishing linewidth. A standard Jaynes-Cummings Hamiltonian is used here to fit the numerical data. The green (blue) dashed lines represent the dipole (quadrupole) mode transmission dip positions. **f** Evolution of the normalized coupling strength  $g/\omega_0$  vs. polarization angle  $\phi$ .

around the FW-BIC region are termed as supercavity resonances.

The dipole–quadrupole strong coupling can be described by a full quantum mechanical Hamiltonian:

$$H = \omega_d(a^\dagger a) + \omega_q(b^\dagger b) + g(a^\dagger + a)(b^\dagger + b) + g^2/\omega_q(a^\dagger + a)^2, \tag{2}$$

where the operators  $a^\dagger(a)$  and  $b^\dagger(b)$  represent the dipole and quadrupole creation (annihilation) terms, respectively. The first two terms of the Hamiltonian describe the dipole and quadrupole individual energies while the second two terms represent the interaction between dipole and quadrupole modes. The Jaynes–Cummings (JC) Hamiltonian also includes counter-rotating interaction terms (CRTs), which can be neglected as an approximation to Eq. (2) (see Supplementary Note 3). Figure 5b presents the best fits to our data with the JC Hamiltonian. At the optimum fitting with Eq. (2), the normalized coupling strength ratio,  $g/\omega_d$ , was determined to be 0.0417 in agreement with the value for  $g/\omega_d$  obtained in Fig. 5. Rabi splitting from the effect of the hybridization of light-matter states can be demonstrated using either classical or quantum approaches and depending on coupling strength lead to very similar results. We emphasize that although our system is essentially classical, we choose to use the quantum approach because it is more inclusive. For example, it provides a unique and clear property of the ultrastrong coupling (USC) regime, such as the breakdown of the rotating waves approximation, which may lead to vacuum Bloch–Siegert shift. However, the spectral response of the system can be equally obtained from a classical description not involving any operator algebra, which is demonstrated above by the finite-difference-time-domain simulations.

Therefore, in a similar fashion to lattice-mediated strong coupling THz metasurfaces<sup>47–50</sup>, one can drive the formation of FW-BIC by capacitance-mediated strong coupling. The advantage of our system over conventional strong light-matter coupling systems is that our system achieves strong coupling with the use of a single structure. In commonly used hybrid light-matter coupling systems, the emitter and cavity are distinct and require a high degree of spatial overlap. As a result, the capacitance-mediated strong coupling scheme not only drives the formation of FW-BIC but also provides flexibility in the engineering to study more exotic physics such as USC with normalized coupling strengths  $>10\%$ <sup>51</sup>.

The possibility to tune the rotation angle  $\phi$  in a continuous way allows to follow the evolution of the dispersion and evaluate the influence of the polarization state of the incident light on the FW-BIC formation. As the polarization angle  $\phi$  is swept, we extract the positions of the minima of sample transmission and plot the dispersion curves for the eigenvalues as a function of the capacitive gap  $c$  (Fig. 6a–e). When  $\phi$  is increased from  $0^\circ$  to  $90^\circ$  ( $0^\circ \leq \phi < 90^\circ$ ), one can observe that the position of the FW-BIC (denoted by a white dashed line) decreases gradually. Indeed, when  $\phi = 0^\circ, 30^\circ, 60^\circ$ , and  $75^\circ$ , respectively, the corresponding widths of the capacitive gaps are 78, 72, 70, and  $68 \mu\text{m}$ , respectively. Here, we attribute this FW-BIC to the degeneracy of the modal asymmetry during the tuning process, which is required by the classical anticrossing. When  $\phi = 90^\circ$ , there is no singularity in the dipole–quadrupole anticrossing since the structural asymmetry is quasi-preserved. In other words, the FW-BIC is completely switched off, which enables completing an ON/OFF cycle. This noticeable tuning of the position of the FW-BIC is accompanied by a linear enhancement of the normalized coupling strength ratio  $g/\omega_0$ , as shown in Fig. 6f. This polarization control of the FW-BIC can be strategically important in developing



optically thin metadevices for quantum information processing in the USC regime.

In summary, we demonstrated two distinct methodologies to drive BICs in THz metasurfaces: (1) linear polarization state of light for SP-BIC and (2) capacitance-mediated strong coupling for FW-BIC. In the first method, SP-BIC is driven by linear polarization state in which the Fano due to asymmetry in  $\alpha = 100\%$  SRR sample is suppressed at polarization angle  $\phi = 30^\circ$ . For the second method, FW-BIC is driven by strong coupling between plasmonic dipole mode and higher order quadrupole mode in an asymmetric SRR ( $\alpha = 100\%$ ) modulated by capacitance. We then demonstrated the polarization dependence of FW-BIC as confirmed by the gradually decreasing capacitive position of FW-BIC with increasing polarization angle  $\phi$ . In addition, FW-BIC is completely switched off at  $\phi = 90^\circ$  which allows for ON/OFF cycling capability. The subwavelength nature of these metasurfaces allows for much smaller mode volume and lifts the dimensional limitations of dielectric photonic crystals<sup>52</sup>. The metadevices studied here have applications in lasing, nonlinear optics, and high-performance sensing devices.

## Methods

**Measurement.** A high-resolution continuous wave THz spectrometer (Teraview CW Spectra 400) that produces linearly polarized collimated terahertz beams was utilized to measure the transmission spectra of the aforementioned fabricated metasurfaces. In this system, the optical beat frequency of two distributed feedback near-IR diode lasers are tuned to produce coherent THz waves between 0.05 and 1.5 THz. The spectral resolution of around 100 MHz is enough to resolve relatively narrow spectral features, in contrast to the limited resolution of time-domain terahertz systems.

Samples were placed equidistant between the emitter and detector in ambient air conditions. After measurement, the transmission spectrum was calculated as  $T(f) = P_M(f)/P_{sub}(f)$ , where  $P_M(f)$  and  $P_{sub}(f)$  are the filtered power spectra of the metasurface and substrate, respectively. For the polarization-dependence investigation, the metamaterial sample is rotated by a value  $\theta$  to mimic the change of a polarization state of the incident beam<sup>53</sup>.

**Simulation.** For numerical simulations, we utilized a finite element method with periodic boundary conditions to simulate a 2D infinite array of unit cells. The length scale of the mesh was set to be less than or equal to  $\lambda_0/10$  throughout the simulation domain, where  $\lambda_0$  is the central wavelength of the incident radiation. The input and output ports are located at  $3\lambda_0$  from the metasurface with open boundary conditions. The material parameters used for the structures are  $\sigma = 4.1 \times 10^7$  S/m for the metallic Ag layer and  $\epsilon = 3.8$  for the dielectric Kapton layer. For the polarization dependent study, each unit cell was excited with a THz plane wave of the correct linear polarization state as indicated by the polarization angle from  $0^\circ$  to  $90^\circ$ .

## Data availability

The data that support the findings of this study are available from the corresponding author upon reasonable request.

Received: 10 February 2020; Accepted: 28 September 2020;

Published online: 18 November 2020

## References

- von Neuman, J. & Wigner, E. Über merkwürdige diskrete Eigenwerte. Über das Verhalten von Eigenwerten bei adiabatischen Prozessen. *Physikalische Zeitschrift* **30**, 467–470 (1929).
- Schult, R. L., Ravenhall, D. G. & Wyld, H. W. Quantum bound states in a classically unbound system of crossed wires. *Phys. Rev. B* **39**, 5476–5479 (1989).
- Exner, P., Šeba, P., Tater, M. & Vanek, D. Bound states and scattering in quantum waveguides coupled laterally through a boundary window. *J. Math. Phys.* **37**, 4867–4887 (1996).
- Parker, R. Resonance effects in wake shedding from parallel plates: some experimental observations. *J. Sound Vib.* **4**, 62–72 (1966).
- Ursell, F. Trapping modes in the theory of surface waves. *Math. Proc. Camb. Philos. Soc.* **47**, 347–358 (1951).
- Watts, M. R., Johnson, S. G., Haus, H. A. & Joannopoulos, J. D. Electromagnetic cavity with arbitrary q and small modal volume without a complete photonic bandgap. *Opt. Lett.* **27**, 1785–1787 (2002).
- Marinica, D. C., Borisov, A. G. & Shabanov, S. V. Bound states in the continuum in photonics. *Phys. Rev. Lett.* **100**, 183902 (2008).
- Molina, M. I., Miroschnichenko, A. E. & Kivshar, Y. S. Surface bound states in the continuum. *Phys. Rev. Lett.* **108**, 070401 (2012).
- Monticone, F. & Alù, A. Embedded photonic eigenvalues in 3d nanostructures. *Phys. Rev. Lett.* **112**, 213903 (2014).
- Hsu, C. W. et al. Observation of trapped light within the radiation continuum. *Nature* **499**, 188–191 (2013).
- Jin, J. et al. Topologically enabled ultrahigh-q guided resonances robust to out-of-plane scattering. *Nature* **574**, 501–504 (2019).
- Li, S., Zhou, C., Liu, T. & Xiao, S. Symmetry-protected bound states in the continuum supported by all-dielectric metasurfaces. *Phys. Rev. A* **100**, 063803 (2019).
- Rybin, M. & Kivshar, Y. Supercavity lasing. *Nature* **541**, 164–165 (2017).
- Ha, S. T. et al. Directional lasing in resonant semiconductor nanoantenna arrays. *Nanotechnol.* **13**, 1042–1047 (2018).
- Kodigala, A. et al. Lasing action from photonic bound states in continuum. *Nature* **541**, 196–199 (2017).
- Contractor, R., Noh, W., Le-Van, Q. & Kanté, B. Doping-induced plateau of strong electromagnetic confinement in the momentum space. *Opt. Lett.* **45**, 3653–3656 (2020).
- Liu, M. et al. Terahertz-field-induced insulator-to-metal transition in vanadium dioxide metamaterial. *Nature* **487**, 345–348 (2012).
- Koshelev, K., Bogdanov, A. & Kivshar, Y. Meta-optics and bound states in the continuum. *Sci. Bull.* **64**, 836–842 (2019).
- Vabishchevich, P. P. et al. Enhanced second-harmonic generation using broken symmetry III–v semiconductor fano metasurfaces. *ACS Photonics* **5**, 1685–1690 (2018).
- Seren, H. R. et al. Nonlinear terahertz devices utilizing semiconducting plasmonic metamaterials. *Light Sci. Appl.* **5**, e16078 (2016).
- Yahiaoui, R. et al. Multispectral terahertz sensing with highly flexible ultrathin metamaterial absorber. *J. Appl. Phys.* **118**, 083103 (2015).
- Evlukhin, A. B. et al. Detuned electrical dipoles for plasmonic sensing. *Nano Lett.* **10**, 4571–4577 (2010).
- Liu, Y., Wang, S., Zhao, D., Zhou, W. & Sun, Y. High quality factor photonic crystal filter at  $k \approx 0$  and its application for refractive index sensing. *Opt. Express* **25**, 10536–10545 (2017).
- Friedrich, H. & Wintgen, D. Interfering resonances and bound states in the continuum. *Phys. Rev. A* **32**, 3231–3242 (1985).
- Azzam, S. I., Shalae, V. M., Boltasseva, A. & Kildishev, A. V. Formation of bound states in the continuum in hybrid plasmonic-photonic systems. *Phys. Rev. Lett.* **121**, 253901 (2018).
- Han, S. et al. All-dielectric active terahertz photonics driven by bound states in the continuum. *Adv. Mater.* **31**, 1901921 (2019).
- Kikkawa, R., Nishida, M. & Kadoya, Y. Polarization-based branch selection of bound states in the continuum in dielectric waveguide modes anti-crossed by a metal grating. *N. J. Phys.* **21**, 113020 (2019).
- Feshbach, H. Unified theory of nuclear reactions. *Ann. Phys.* **5**, 357–390 (1958).
- Yoon, J. W., Song, S. H. & Magnusson, R. Critical field enhancement of asymptotic optical bound states in the continuum. *Sci. Rep.* **5**, 18301 (2015).
- Cong, L. & Singh, R. Symmetry-protected dual bound states in the continuum in metamaterials. *Adv. Opt. Mater.* **7**, 1900383 (2019).
- Abujetas, D. R., van Hoof, N., ter Huurne, S., Rivas, J. G. & Sánchez-Gil, J. A. Spectral and temporal evidence of robust photonic bound states in the continuum on terahertz metasurfaces. *Optica* **6**, 996–1001 (2019).
- Fan, K., Shadrivov, I. V. & Padilla, W. J. Dynamic bound states in the continuum. *Optica* **6**, 169–173 (2019).
- Zhang, W., Charous, A., Nagai, M., Mittleman, D. M. & Mendis, R. Extraordinary optical reflection resonances and bound states in the continuum from a periodic array of thin metal plates. *Opt. Express* **26**, 13195–13204 (2018).
- Pankin, P. S. et al. One-dimensional photonic bound states in the continuum. *Commun. Phys.* **3**, 91 (2020).
- Singh, R., Al-Naib, I., Koch, M. & Zhang, W. Sharp fano resonances in thz metamaterials. *Opt. Express* **19**, 6312–6319 (2011).
- Cong, L. et al. Fano resonances in terahertz metasurfaces: a figure of merit optimization. *Adv. Opt. Mater.* **3**, 1537–1543 (2015).
- Manjappa, M. et al. Tailoring the slow light behavior in terahertz metasurfaces. *Appl. Phys. Lett.* **106**, 181101 (2015).
- Srivastava, Y. K. et al. Ultrahigh-q fano resonances in terahertz metasurfaces: strong influence of metallic conductivity at extremely low asymmetry. *Adv. Opt. Mater.* **4**, 457–463 (2015).
- Fedotov, V. A., Rose, M., Prosvirnin, S. L., Papasimakis, N. & Zheludev, N. I. Sharp trapped-mode resonances in planar metamaterials with a broken

- structural symmetry. *Phys. Rev. Lett.* **99**, <https://doi.org/10.1103/PhysRevLett.99.147401> (2007).
40. Singh, R., Al-Naib, I., Koch, M. & Zhang, W. Asymmetric planar terahertz metamaterials. *Opt. Express* **18**, 13044–13050 (2010).
  41. Singh, R. et al. Observing metamaterial induced transparency in individual fano resonators with broken symmetry. *Appl. Phys. Lett.* **99**, 201107 (2011).
  42. Koshelev, K., Lepeshov, S., Liu, M., Bogdanov, A. & Kivshar, Y. Asymmetric metasurfaces with high-q resonances governed by bound states in the continuum. *Phys. Rev. Lett.* **121**, 193903 (2018).
  43. Al-Naib, I. et al. Excitation of a high-q subradiant resonance mode in mirrored single-gap asymmetric split ring resonator terahertz metamaterials. *Appl. Phys. Lett.* **101**, 071108 (2012).
  44. Gupta, M. et al. Sharp toroidal resonances in planar terahertz metasurfaces. *Adv. Mater.* **28**, 8206–8211 (2016).
  45. Al-Naib, I., Yang, Y., Dignam, M. M., Zhang, W. & Singh, R. Ultra-high q even eigenmode resonance in terahertz metamaterials. *Appl. Phys. Lett.* **106**, <https://doi.org/10.1063/1.4905478> (2015).
  46. Hsu, C. W., DeLacy, B. G., Johnson, S. G., Joannopoulos, J. D. & Soljačić, M. Theoretical criteria for scattering dark states in nanostructured particles. *Nano Lett.* **14**, 2783–2788 (2014).
  47. Burrow, J. A. et al. Eigenmode hybridization enables lattice-induced transparency in symmetric terahertz metasurfaces for slow light applications. *Opt. Lett.* **44**, 2705–2708 (2019).
  48. Zhao, Z., Zhao, H., Ako, R. T., Nickl, S. & Sriram, S. Polarization-insensitive terahertz spoof localized surface plasmon-induced transparency based on lattice rotational symmetry. *Appl. Phys. Lett.* **117**, 011105 (2020).
  49. Manjappa, M., Srivastava, Y. K. & Singh, R. Lattice-induced transparency in planar metamaterials. *Phys. Rev. B* **94**, 161103 (2016).
  50. Keller, J. et al. Coupling surface plasmon polariton modes to complementary thz metasurfaces tuned by inter meta-atom distance. *Adv. Opt. Mater.* **5**, 1600884 (2017).
  51. Forn-Díaz, P., Lamata, L., Rico, E., Kono, J. & Solano, E. Ultrastrong coupling regimes of light-matter interaction. *Rev. Mod. Phys.* **91**, 025005 (2019).
  52. Kyaw, C. et al. Guided-mode resonances in flexible 2d terahertz photonic crystals. *Optica* **7**, 537–541 (2020).
  53. Burrow, J. A. et al. Polarization-dependent electromagnetic responses of ultrathin and highly flexible asymmetric terahertz metasurfaces. *Opt. Express* **25**, 32540–32549 (2017).

## Acknowledgements

This project is supported by the W. M. Keck Foundation, the National Science Foundation (NSF) under NSF award nos. 1541959 and 1659224, Air Force Office of Scientific

Research (FA9550-16-1-0346), and the NASA Ohio Space Grant (NNX15AL50H). C.K. acknowledges support from the Just-Julian Fellowship Program at Howard University and T.A.S. acknowledges support from the CNS Scholars Program. We also thank Boubacar Kante and Rushin Contractor for fruitful discussion.

## Author contributions

C.K., V.T., and R.Y. performed numerical simulations in this study under the supervision of T.A.S. J.A.B., K.K., and W.S. fabricated and characterized the samples under the supervision of E.R., A.S., W.S.R., M.A.T., I.A., and T.A.S. All authors contributed to the discussions of the work and the paper was primarily written and edited by C.K., R.Y., and T.A.S.

## Competing interests

The authors declare no competing interests.

## Additional information

**Supplementary information** is available for this paper at <https://doi.org/10.1038/s42005-020-00453-8>.

**Correspondence** and requests for materials should be addressed to T.A.S.

**Reprints and permission information** is available at <http://www.nature.com/reprints>

**Publisher's note** Springer Nature remains neutral with regard to jurisdictional claims in published maps and institutional affiliations.



**Open Access** This article is licensed under a Creative Commons Attribution 4.0 International License, which permits use, sharing, adaptation, distribution and reproduction in any medium or format, as long as you give appropriate credit to the original author(s) and the source, provide a link to the Creative Commons license, and indicate if changes were made. The images or other third party material in this article are included in the article's Creative Commons license, unless indicated otherwise in a credit line to the material. If material is not included in the article's Creative Commons license and your intended use is not permitted by statutory regulation or exceeds the permitted use, you will need to obtain permission directly from the copyright holder. To view a copy of this license, visit <http://creativecommons.org/licenses/by/4.0/>.

© The Author(s) 2020